Science Advances
AAAS

Supplementary Materials for

Exploiting extraordinary topological optical forces at bound states in the continuum

Haoye Qin *et al.*

Corresponding author: Yuzhi Shi, yuzhi_shi01@163.com; Patrice Genevet, patrice.genevet@crhea.cnrs.fr; Qinghua Song, song.qinghua@sz.tsinghua.edu.cn

Sci. Adv. **8**, eade7556 (2022)
DOI: 10.1126/sciadv.ade7556

This PDF file includes:

Supplementary Note 1: Optical force in the *z*-direction

Figure S1 evaluates the optical force in *z* direction around the BIC with the nanosphere having a *z* displacement of 1000 nm above the PhCS. Figs. S1A,B show the sign value of F_z for the upper and lower band. The optical force F_z is negative within a circle region around the BIC and becomes positive outside this region. The relevant absolute value of optical force F_z is shown in Figs. S1C,D, normalized to a value of $F_0 = 10^{-16}$ N. Fig. S1E evaluates the net force defined as the buoyant force from water minus the nanosphere's gravity. When varying the density of the polymer nanosphere from 0.7 to 1.3, the net force will gradually change from positive to negative. For practical consideration, there will be a match between the net force and optical force F_z by tuning material density and nanosphere radius for stable levitation in *z* direction.

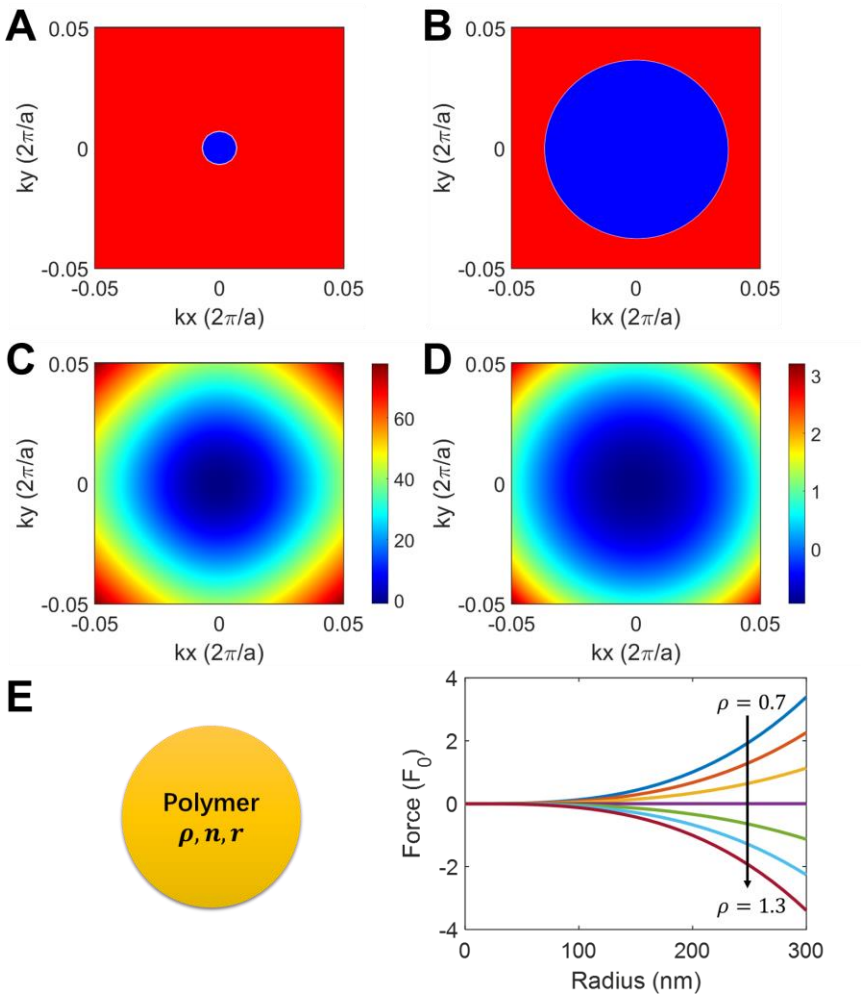

Figure S1. Evaluation of force in *z* direction. Sign value of optical force in *z* direction for the (**A**) upper band and (**B**) lower band. Absolute value of optical force in *z* direction normalized to a value of $F_0 = 10^{-16}$ N for the (**C**) upper band and (**D**) lower band. (**E**) Net force of the polymer nanosphere when varying the material density and radius.

Supplementary Note 2: Effect of displacement in the *z*-direction on topological distribution of optical force.

To evaluate the effect of displacement in *z* direction on topological distribution of optical force, the nanosphere is positioned at 900 nm and 1100 nm above the PhCS. Optical force distribution is obtained in Fig. S2. At the position of 900 nm in Figs. S2A-D, BIC on both lower band and upper band generates converging force pattern that attracts objects to the center. The corresponding angle of force vector is shown in Figs. S2C,D with the same topological distribution. In Figs. S2E-H, the nanosphere is placed at a distance of 1100 nm, and both BICs induce diverging force pattern that drives objects away from the center. The same topology for both band is manifested in Figs. S2G,H, with a difference of 180° between the two displacement in *z* direction.

Figure S3 demonstrates the relation between *z* displacement and converging and diverging pattern of the topological force. The force direction in the first quadrant in momentum space is characterized by $sign[F_{x,y}]$, that is, $F_{x,y} > 0$, the value is 1; $F_{x,y} < 0$, the value is -1. To realize converging pattern on one band and diverging pattern on the other band, the two band cannot have the same value for one position. When sphere position in *z* direction is placed between 975 nm and 1050 nm, switch from converging to diverging pattern can be achieved by changing frequency band (indicated by a double arrow, as demonstrated in the main text). For the *z* displacement is smaller than 975 nm, the red arrow indicates both bands have converging force pattern as demonstrated in Figs. S2A-D. For the *z* displacement is larger than 1050 nm, the blue arrow indicates both bands have diverging force pattern as demonstrated in Figs. S2E-H.

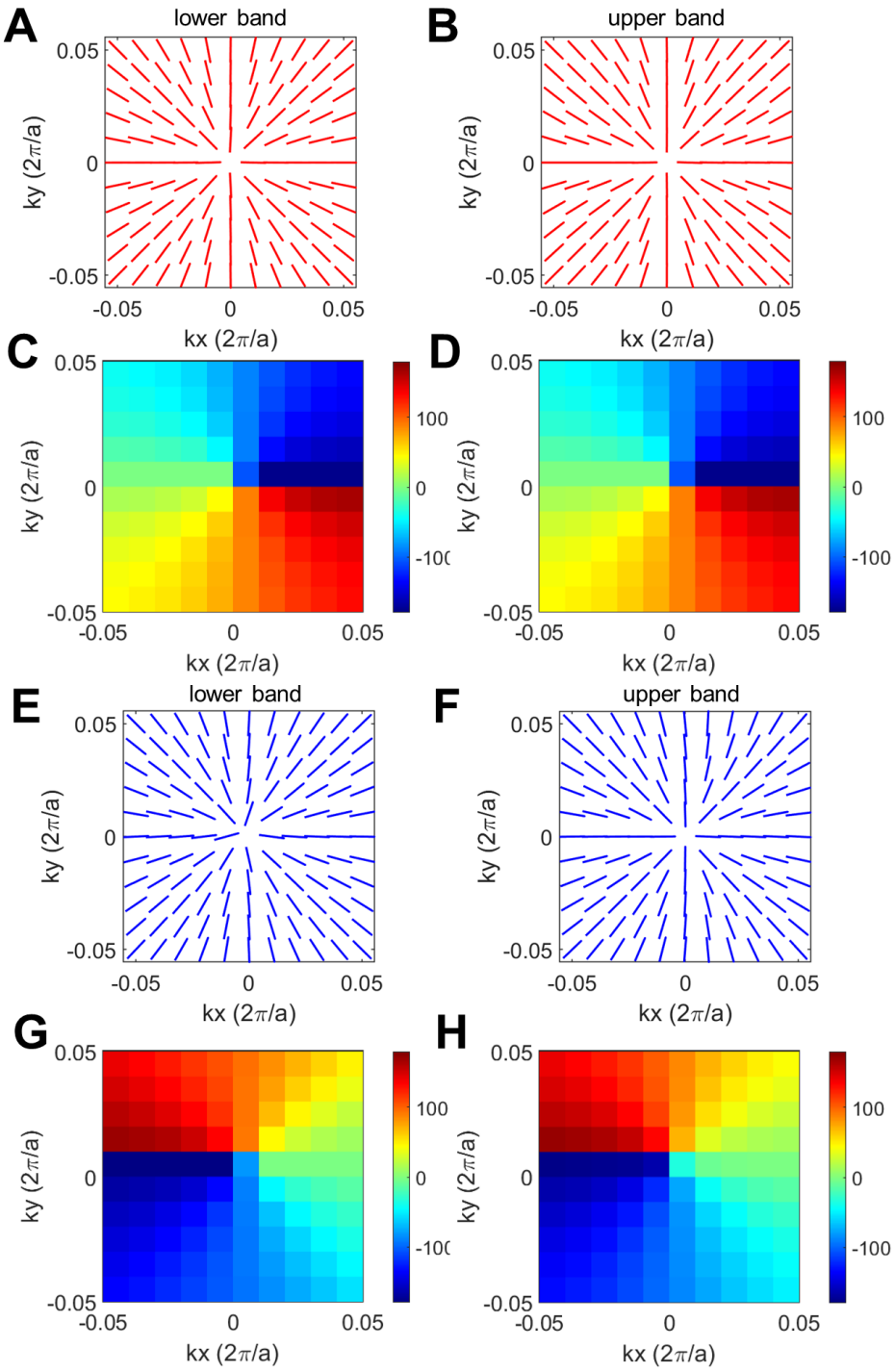

Figure S2. Topological force distribution with different *z* distance of nanosphere above the PhCS. (**A**-**D**) *z* = 900 nm and (**E**-**H**) *z* = 1100 nm. (**A**, **E**) and (**B**, **F**) are the force distribution for lower and upper band, respectively. (**C**, **G**) and (**D**, **H**) show the corresponding map of angle of the force vector.

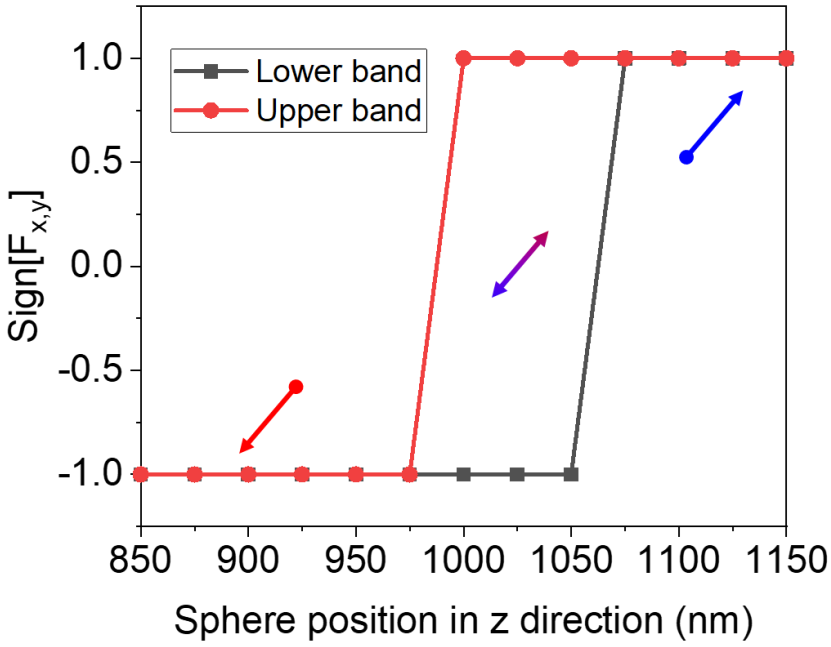

Figure S3. The value of *sign*[$F_{x,y}$] in the first quadrant as a function of sphere position in *z* direction for the upper band and lower band. The arrows indicate the converging and diverging pattern of the force topology.

Supplementary Note 3: Evolution of the force zero with displacement of nanosphere in the *x*-direction.

Figure S4 shows the evolution of force zero for the lower band when displacing the nanosphere in *x* direction. When moving the nanosphere to the negative position of *x* axis, the force zero will change to the position of positive k_x (Fig. S4A). In Figs. S4B-D, the nanosphere is continuously moved to positive position of *x* axis with a distance of 50, 100, and 150 nm. The corresponding force zero shifts more far away from the Γ point to offset the displacement of the nanosphere. With in-plane displacement of the nanosphere, force topology is maintained and the nanosphere will always perceive a force pointing to the Γ point until the force zero and nanosphere position coincide at the center. Fig. S5 shows the effect of nanoparticles for the eigenmodes of the PhCS with BIC. The resonant frequency and quality factor of the PhCS remain the same when there are nanoparticles above the PhCS at a distance of 1 um and when there is only the PhCS. Therefore, we verify that the nanoparticles placed above the PhCS will not induce changes in the optical response (resonance position, modulation, quality factor) of the PhCS. Obviously, the movement of the nanosphere has no effect on the eigenmode of lower band. Due to the large contrast in the shape, size, and index of the PhCS and nanosphere, the eigenfrequencies corresponding to the eigenmodes of the PhCS and nanoparticle are very different. Thus, the mutual coupling between PhCS and nanosphere is negligible.

The upper band has similar trend as shown in Fig. S6 with a displacement of 50 nm in the positive *x*-axis direction. Fig. S6A shows the force distribution in momentum space and two force zeros occur with the left one being the shifted force zero from Γ point. The two force zeros have different topological pattern. The left one is enclosed by converging force that attracts nanoparticles, while the right one is dragging objects in *y* direction and pulling them away in *x* direction. Topological feature of the two force zeros is illustrated in Fig. S6B, with the force vector winding around the zeros in opposite direction. Fig. S4C and Fig. S4D show the value of $sign[F_x]$ and $sign[F_y]$ for showing the direction force in momentum space, respectively.

Evolution of the force zero with varying *x* displacement at 50,100, 150 nm and -50 nm are shown in Figs. S7A-D. The left force zero in Fig. S7A will shift outside the view and leave only the right force zero in Figs. S7B, C. The force distribution pattern of Fig. 7B is given in Fig. S7E. This force zero is enclosed by *y* converging and *x* diverging force pattern, as indicated by the four blue arrows showing force direction. Angle of the force vector in momentum space is plotted in Fig. S6F.

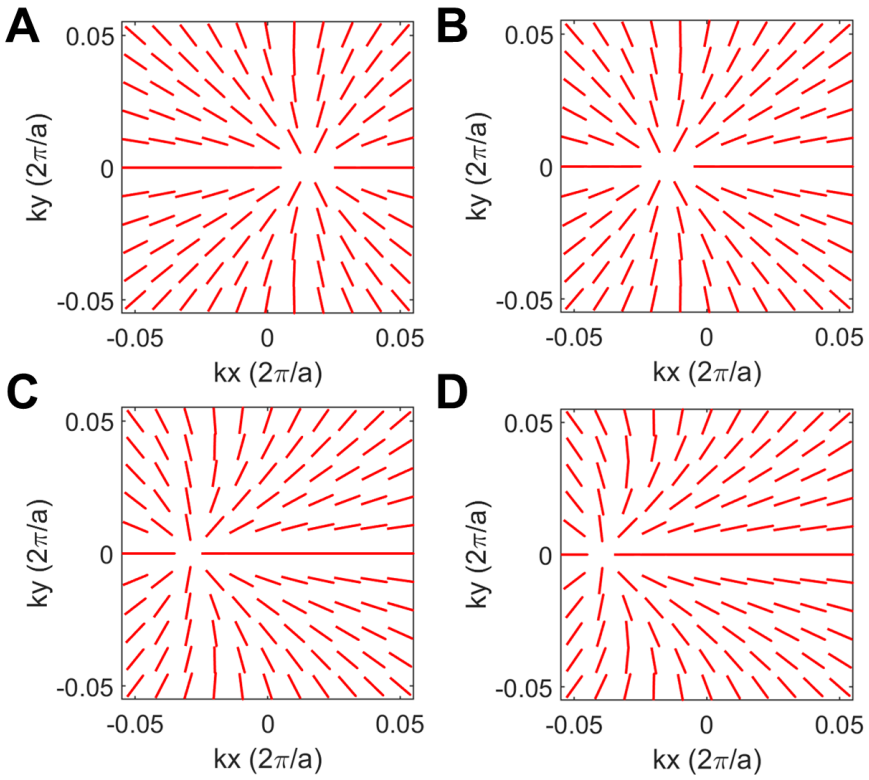

Figure S4. Force zero for the lower band with displacement of nanosphere in *x* direction. The *x* displacement is -50, 50, 100, and 150 nm for (A-D).

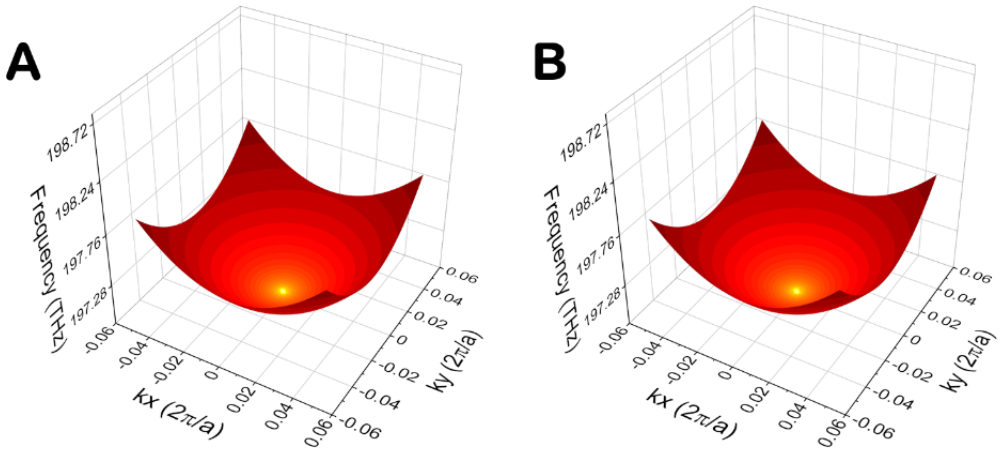

Figure S5. Effect of nanosphere on the eigenmode. The calculated lower-band iso-frequency surface and color-mapped quality factor of the PhCS (A) with nanoparticles and (B) without nanoparticles positioned above the PhCS at a distance of 1 um.

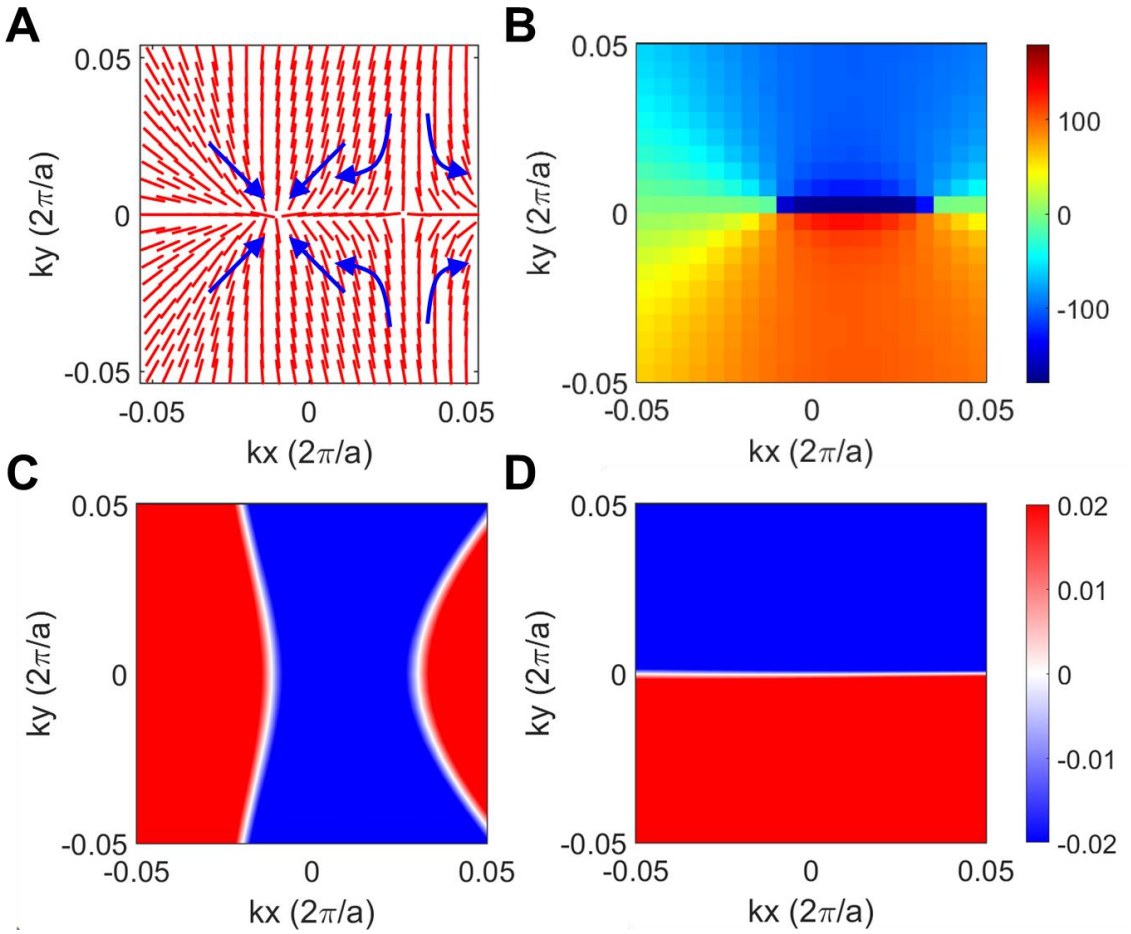

Figure S6. Force topology for the upper band with nanosphere displacement of 50 nm in *x* direction. (**A**) Force distribution with two force zeros showing different topology. The arrows indicate the flow direction of objects when placed in the force pattern. (**B**) Map of angle of the force vector. Map of sign value of optical force in (**C**) *x* direction and (**D**) *y* direction.

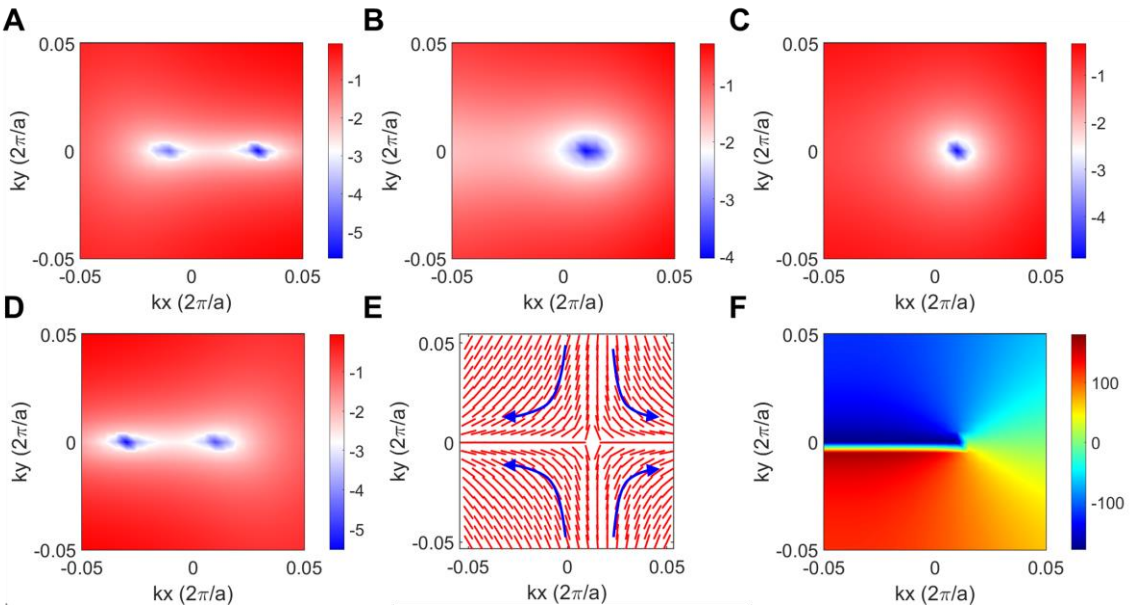

Figure S7. Topological force distribution with *x* displacement. (**A**-**D**) Absolute value of optical force in log scale shows the distribution of force zeros on the upper band for *x* displacement of -50, 50, 100, and 150 nm. (**E**) Pattern of force distribution for (**B**) with the arrows showing the flow direction. (**F**) Map of angle of the force vector for (**E**).

Supplementary Note 4: Robustness of topological force against size and refractive index of the nanosphere

Figure S8 evaluates the robustness of topological force when varying the size of nanosphere to radius of 50 nm for Figs. S8A, C and radius of 200 nm for Figs. S8B, D. The top row is the lower band showing converging force topology and the bottom row is the upper band showing diverging force topology. In Fig. S9, the refractive index of the nanosphere is modified to 1.4 for Figs. S9A, C and 1.8 for Figs. S9B, D. The top row is the lower band with converging force topology and the bottom row is the upper band with diverging force topology. Therefore, the topological force is very robust against size and refractive index of the nanosphere.

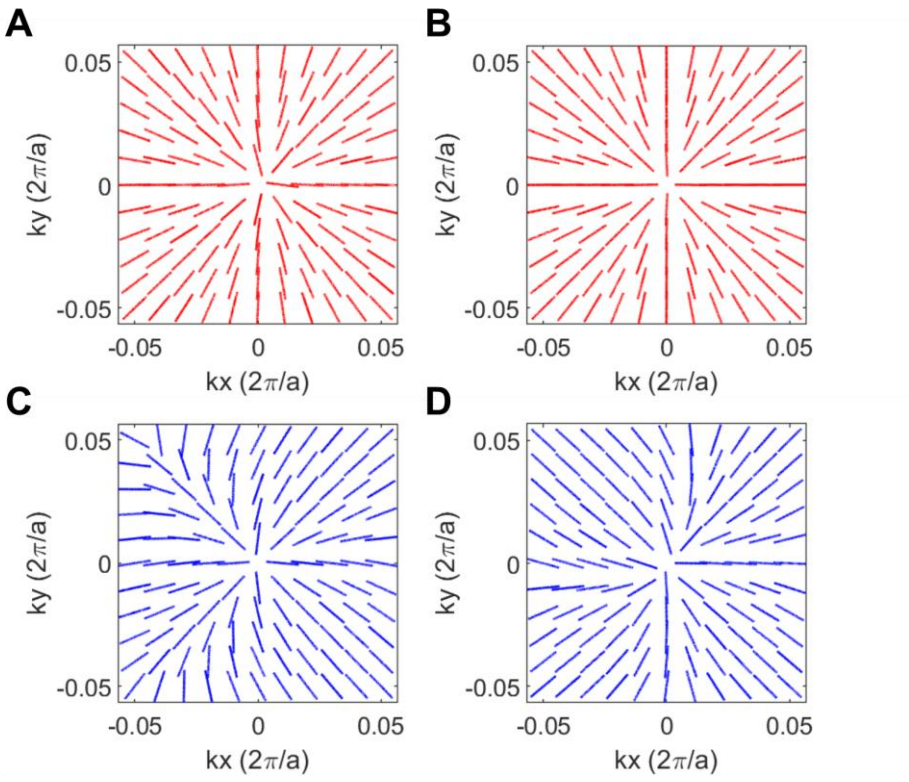

Figure S8. Effect of size of nanosphere on the topological force. Converging force pattern for the nanosphere with radius of (**A**) 50 nm and (**B**) 200 nm. Diverging force pattern for the nanosphere with radius of (**C**) 50 nm and (**D**) 200 nm.

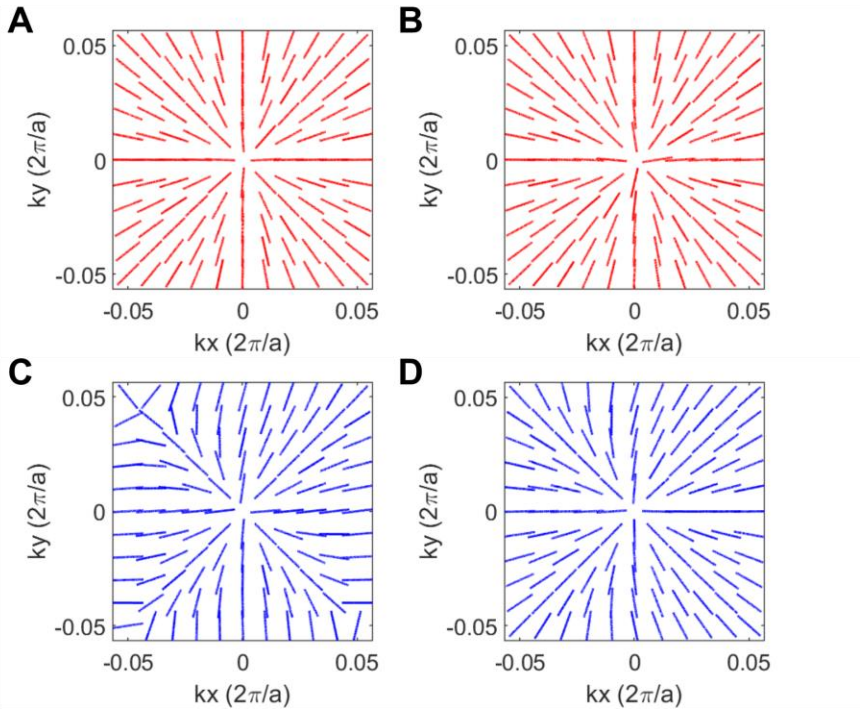

Figure S9. Effect of refractive index of nanosphere on the topological force. Converging force pattern for the nanosphere with refractive index of (**A**) 1.4 and (**B**) 1.8. Diverging force pattern for the nanosphere with radius of (**C**) 1.4 and (**D**) 1.8.

Supplementary Note 5: Three-dimensional trapping with *x*-shifted PhCS

When the top and bottom hole has displacement in *x* direction by 5 nm, the force zero around lower-band BIC will shift to positive for objects above the PhCS (Fig. S10A) and to negative for objects below the PhCS (Fig. S10B). This asymmetric force distribution for objects in different position may be employed for achieving three-dimensional trapping and manipulation.

As demonstrated in Fig. S10, by shifting the hole of two layers in opposite *x*-direction, the nanosphere can be trapped at off-Γ point with the converging force pattern. Here, we propose a three-dimensional trapping mechanism for trapping objects at different positions in the *xy* plane for different values *z* distance above and below the PhCS. The two holes are shifted individually in *x* direction with a displacement of 5 nm (Fig. S10). Fig. S10 illustrates the evolution of trapping position as a function of *z* distance. Above the PhCS, increasing the *z* distance from 880 nm to 980 nm, the trapping position (force zero in a converging force pattern) will evolve from a point at positive k_x to negative k_x, crossing Γ point in the process. Below the PhCS, the trapping positions will have a mirror symmetric position with the case above the PhCS.

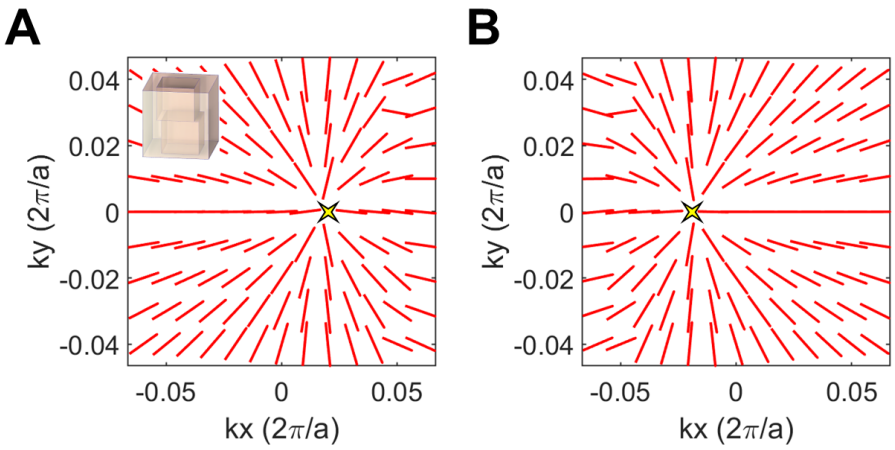

Figure S10. Topological force distribution with displaced PhCS. Force distribution (**A**) above the PhCS and (**B**) below the PhCS around lower-band BIC when the PhCS has the holes displaced in direction by 5 nm.

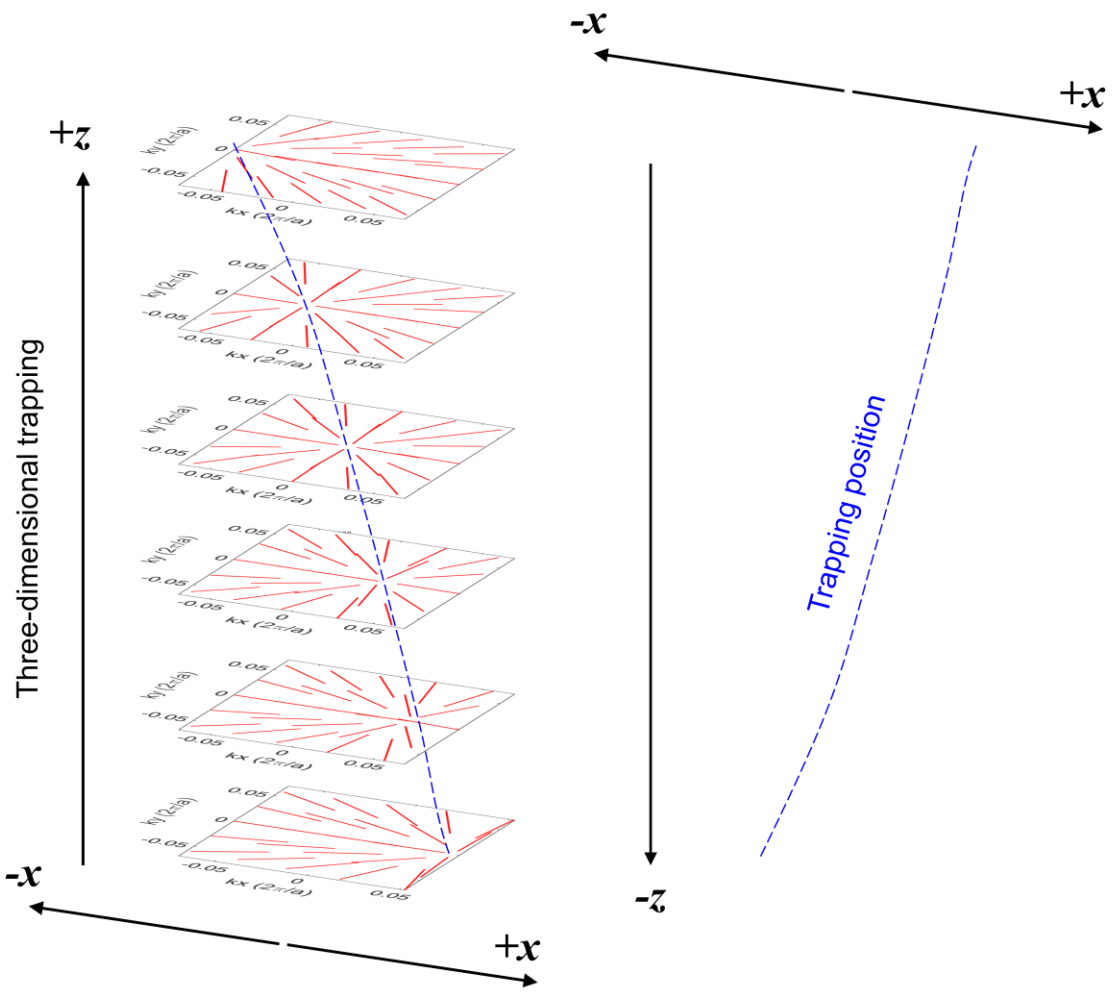

Figure S11. Schematic of the proposed three-dimensional trapping with *x*-shifted PhCS for trapping position above and below the PhCS.

Supplementary Note 6: Field decomposition

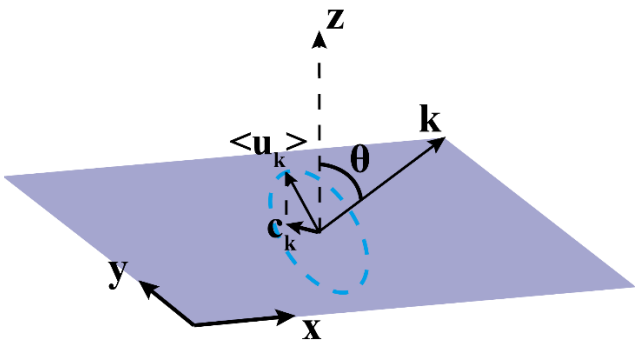

Figure S12. Schematics of radiation field decomposition for resonances of PhCS. When external light is incident on the PhCS to excite the resonance mode, the excited mode radiates outward to form the far-field polarization. We decompose the far-field polarization into the *x*-*y* plane, as shown in Fig. S12. According to Bloch theorem for photonic crystals, the electric field of resonance can be written as $\mathbf{E}_{\mathbf{k}_{\|}}(\rho,z)=e^{i\mathbf{k}_{\|}\cdot\boldsymbol{\rho}}\mathbf{u}_{\mathbf{k}_{\|}}(\rho,z)$. Here, $\mathbf{k}_{\|}=\mathbf{k}\sin(\theta)=k_x\hat{x}+k_y\hat{y}$ is the in-plane wave vector, $\boldsymbol{\rho}=x\hat{x}+y\hat{y}$ is the in-plane coordinate, $\mathbf{u_k}$ is periodic function in ρ, and z is the normal direction. Then, we project $\mathbf{u_k}$ into the x-y plane through $c_{k_{\|}}=\boldsymbol{\rho}\bullet\langle\mathbf{u_k}\rangle$, where the brackets denote the spatial average over one unit cell on any horizontal plane outside the PhCS (*1*). Similarly, we can decompose the magnetic field of resonance into the *x*-*y* plane. By the equation (1) and (2) in the manuscript, the in-plane force vector distribution can be obtained. Based on the relation between the spatial angle θ and in-plane vector $k_{\|}$, the proposed topological feature of optical force distribution can be realized not only in momentum space but also in real space.

Supplementary Note 7: Geometrical parameters for BIC

We note the lattice periodicity, hole side length, and thickness of the PhCS may affect the BIC. The lattice periodicity of 574 nm is chosen for approaching the BIC condition around the frequency of 200 THz. While for other wavelength or frequency, the lattice periodicity and hole side length can be accordingly scaled to realize BIC at the targeted value. These geometrical parameters are suitable for nanofabrication. Fig. S13 demonstrates the impact of geometrical parameters on the BIC. With a fixed side length of the square hole at 330 nm, we change the lattice periodicity away from 574 nm and the quality factor is relatively stable for both lower mode and upper mode in Fig. S13(a,b). The value of 574 nm is chosen to allow more tolerance for possible fabrication imperfection. Fig. S13(c) compares the quality factor as a function of *k*-vector for different values of lattice periodicity, and the lattice periodicity of 574 nm has a larger quality factor at *k*-vector equal to zero. The impact of side length of the square hole on quality factor is evaluated in Fig. S13(d), from which we can see a deviation of the side length within a limited range doesn't affect the BIC very much.

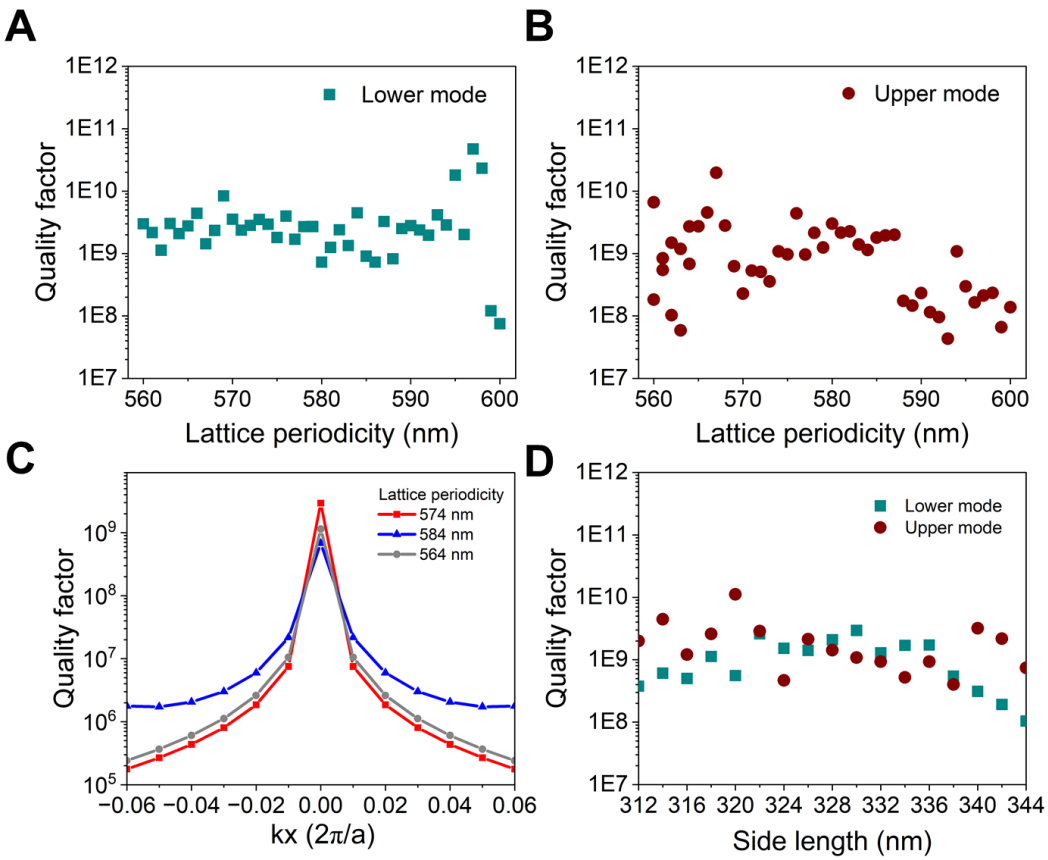

Figure S13. Evaluation of geometrical parameters on the BIC. Impact of lattice periodicity on the quality factor at BIC for (A) the lower mode and (B) the upper mode. (C) The quality factor in *k* space at different values of lattice periodicity for the lower mode. (D) Impact of side length on the quality factor at BIC.

Supplementary Note 8: Possibility of enhancing the optical force

In order to enhance the optical force, the most direct way is increasing the excitation power and since the PhCS operates around BIC with high field localization, the optical forces should be larger than those without BIC. And there may be three potential methods to enhance the induced optical force by promoting fields of the PhCS platform. The first method is to introduce epsilon-near-zero (ENZ) materials, such as Indium Tin Oxide (ITO), Aluminum doped Zinc Oxide (AZO), Gallium doped Zinc Oxide (GZO) and Fluorine doped Tin Oxide (FTO). According to the conservation of the electric displacement vector, the electric field localization can be greatly enhanced (*40*),and this method is also used in several articles (*41*, *42*). The second method is to suppress the lateral radiation of BIC by changing the periodic boundary condition to photonic bandgap boundary condition(*10*). The third method is to construct merging BIC by tuning multiple fundamental BICs to merge at a chosen *k* point (*5*,*43*,*44*).

REFERENCES AND NOTES

1. B. Zhen, C. W. Hsu, L. Lu, A. D. Stone, M. Soljačić, Topological nature of optical bound states in the continuum. *Phys. Rev. Lett.* **113**, 1–5 (2014).

2. L. Shi, Y. Kivshar, W. Liu, W. Liu, Topological polarization singularities in metaphotonics. *Nanophotonics* **10**, 1469–1486 (2021).

3. Y. Zhang, A. Chen, W. Liu, C. W. Hsu, B. Wang, F. Guan, X. Liu, L. Shi, L. Lu, J. Zi, Observation of polarization vortices in momentum space. *Phys. Rev. Lett.* **120**, 186103 (2018).

4. C. W. Hsu, B. Zhen, A. D. Stone, J. D. Joannopoulos, M. Soljacic, Bound states in the continuum. *Nat. Rev. Mater.* **1**, 16048 (2016).

5. J. Jin, X. Yin, L. Ni, M. Soljačić, B. Zhen, C. Peng, Topologically enabled ultrahigh-Q guided resonances robust to out-of-plane scattering. *Nature* **574**, 501–504 (2019).

6. H. M. Doeleman, F. Monticone, W. den Hollander, A. Alù, A. F. Koenderink, Experimental observation of a polarization vortex at an optical bound state in the continuum. *Nat. Photonics* **12**, 397–401 (2018).

7. T. Bai, Q. Li, Y. Wang, Y. Chen, Z.-D. Hu, J. Wang, Terahertz vortex beam generator based on bound states in the continuum. *Opt. Express* **29**, 25270–25279 (2021).

8. S. Joseph, S. Pandey, S. Sarkar, J. Joseph, Bound states in the continuum in resonant nanostructures: An overview of engineered materials for tailored applications. *Nanophotonics* **10**, 4175–4207 (2021).

9. S. Mohamed, J. Wang, H. Rekola, J. Heikkinen, B. Asamoah, L. Shi, T. K. Hakala, Controlling topology and polarization state of lasing photonic bound states in continuum. *Laser Photon. Rev.* **16**, 2100574 (2022).

10. Z. Chen, X. Yin, J. Jin, Z. Zheng, Z. Zhang, F. Wang, L. He, B. Zhen, C. Peng, Observation of miniaturized bound states in the continuum with ultra-high quality factors. *Sci. Bull.* **67**, 359–366 (2022).

11. B. Wang, W. Liu, M. Zhao, J. Wang, Y. Zhang, A. Chen, F. Guan, X. Liu, L. Shi, J. Zi, Generating optical vortex beams by momentum-space polarization vortices centred at bound states in the continuum. *Nat. Photonics* **14**, 623–628 (2020).

12. A. Kodigala, T. Lepetit, Q. Gu, B. Bahari, Y. Fainman, B. Kanté, Lasing action from photonic bound states in continuum. *Nature* **541**, 196–199 (2017).

13. L. Kang, Y. Wu, X. Ma, S. Lan, D. H. Werner, High-harmonic optical vortex generation from photonic bound states in the continuum. *Adv. Opt. Mater.* **10**, 2101497 (2022).

14. Y. Wu, L. Kang, D. H. Werner, Active quasi-BIC optical vortex generators for ultrafast switching. *New J. Phys.* **24**, 033002 (2022).

15. C. Huang, C. Zhang, S. Xiao, Y. Wang, Y. Fan, Y. Liu, N. Zhang, G. Qu, H. Ji, J. Han, L. Ge, Y. Kivshar, Q. Song, Ultrafast control of vortex microlasers. *Science* **367**, 1018–1021 (2020).

16. W. Liu, B. Wang, Y. Zhang, J. Wang, M. Zhao, F. Guan, X. Liu, L. Shi, J. Zi, Circularly polarized states spawning from bound states in the continuum. *Phys. Rev. Lett.* **123**, 116104 (2019).

17. T. Yoda, M. Notomi, Generation and annihilation of topologically protected bound states in the continuum and circularly polarized states by symmetry breaking. *Phys. Rev. Lett.* **125**, 053902 (2020).

18. Y. Zeng, G. Hu, K. Liu, Z. Tang, C. W. Qiu, Dynamics of topological polarization singularity in momentum space. *Phys. Rev. Lett.* **127**, 176101 (2021).

19. W. Ye, Y. Gao, J. Liu, Singular points of polarizations in the momentum space of photonic crystal slabs. *Phys. Rev. Lett.* **124**, 153904 (2020).

20. D. Andrén, D. G. Baranov, S. Jones, G. Volpe, R. Verre, M. Käll, Microscopic metavehicles powered and steered by embedded optical metasurfaces. *Nat. Nanotechnol.* **16**, 970–974 (2021).

21. O. Ilic, H. A. Atwater, Self-stabilizing photonic levitation and propulsion of nanostructured macroscopic objects. *Nat. Photonics* **13**, 289–295 (2019).

22. Y. Y. Tanaka, P. Albella, M. Rahmani, V. Giannini, S. A. Maier, T. Shimura, Plasmonic linear nanomotor using lateral optical forces. *Sci. Adv.* **6**, eabc3726 (2020).

23. M. Liu, T. Zentgraf, Y. Liu, G. Bartal, X. Zhang, Light-driven nanoscale plasmonic motors. *Nat. Nanotechnol.* **5**, 570–573 (2010).

24. Y. Shi, Q. Song, I. Toftul, T. Zhu, Y. Yu, W. Zhu, P. Tsai, Y. Kivshar, A. Q. Liu, Optical manipulation with metamaterial structures. *Appl. Phys. Rev.* **9**, 031303 (2022).

25. R. Quidant, A light ride to the stars. *Nat. Photonics* **13**, 227–228 (2019).

26. H. A. Atwater, A. R. Davoyan, O. Ilic, D. Jariwala, M. C. Sherrott, C. M. Went, W. S. Whitney, J. Wong, Materials challenges for the Starshot lightsail. *Nat. Mater.* **17**, 861–867 (2018).

27. O. Ilic, I. Kaminer, B. Zhen, O. D. Miller, H. Buljan, M. Soljačić, Topologically enabled optical nanomotors. *Sci. Adv.* **3**, 1–8 (2017).

28. X. Wu, R. Ehehalt, G. Razinskas, T. Feichtner, J. Qin, B. Hecht, Light-driven microdrones. *Nat. Nanotechnol.* **17**, 477–484 (2022).

29. T. van Leest, J. Caro, Cavity-enhanced optical trapping of bacteria using a silicon photonic crystal. *Lab Chip* **13**, 4358–4365 (2013).

30. A. S. Ang, S. V. Sukhov, A. Dogariu, A. S. Shalin, Scattering forces within a left-handed photonic crystal. *Sci. Rep.* **7**, 41014 (2017).

31. S. Yang, C. Hong, Y. Jiang, J. C. Ndukaife, Nanoparticle trapping in a quasi-BIC system. *ACS Photonics* **8**, 1961–1971 (2021).

32. Y. Shi, Y. Wu, L. K. Chin, Z. Li, J. Liu, M. K. Chen, S. Wang, Y. Zhang, P. Y. Liu, X. Zhou, H. Cai, W. Jin, Y. Yu, R. Yu, W. Huang, P. H. Yap, L. Xiao, W. Ser, T. T. B. Nguyen, Y. T. Lin, P. C. Wu, J. Liao, F. Wang, C. T. Chan, Y. Kivshar, D. P. Tsai, A. Q. Liu, Multifunctional virus manipulation with large-scale arrays of all-dielectric resonant nanocavities. *Laser Photon. Rev.* **16**, 2100197 (2022).

33. H. Li, Y. Cao, L.-M. Zhou, X. Xu, T. Zhu, Y. Shi, C.-W. Qiu, W. Ding, Optical pulling forces and their applications. *Adv. Opt. Photonics* **12**, 288 (2020).

34. Q. Song, M. Odeh, J. Zúñiga-Pérez, B. Kanté, P. Genevet, Plasmonic topological metasurface by encircling an exceptional point. *Science* **373**, 1133–1137 (2021).

35. C. W. Hsu, B. Zhen, J. Lee, S. L. Chua, S. G. Johnson, J. D. Joannopoulos, M. Soljačić, Observation of trapped light within the radiation continuum. *Nature* **499**, 188–191 (2013).

36. Q. Song, A. Baroni, P. C. Wu, S. Chenot, V. Brandli, S. Vézian, B. Damilano, P. D. Mierry, S. Khadir, P. Ferrand, P. Genevet, Broadband decoupling of intensity and polarization with vectorial Fourier metasurfaces, *Nat. Commun.* **12**, 3631 (2021).

37. H. Moriceau, F. Rieutord, F. Fournel, Y. le Tiec, L. di Cioccio, C. Morales, A. M. Charvet, C. Deguet, Overview of recent direct wafer bonding advances and applications. *Adv. Nat. Sci. Nanosci. Nanotechnol.* **1**, 043004 (2010).

38. K. Tanaka, D. Arslan, S. Fasold, M. Steinert, J. Sautter, M. Falkner, T. Pertsch, M. Decker, I. Staude, Chiral bilayer all-dielectric metasurfaces. *ACS Nano* **14**, 15926–15935 (2020).

39. T. Stolt, J. Kim, S. Héron, A. Vesala, Y. Yang, J. Mun, M. Kim, M. J. Huttunen, R. Czaplicki, M. Kauranen, J. Rho, P. Genevet, Backward phase-matched second-harmonic generation from stacked metasurfaces. *Phys. Rev. Lett.* **126**, 033901 (2021).

40. M. Z. Alam, I. de Leon, R. W. Boyd, Large optical nonlinearity of indium tin oxide in its epsilon-near-zero region. *Science* **352**, 795–797 (2016).

41. X. Zhang, Y. Liu, J. Han, Y. Kivshar, Q. Song, Chiral emission from resonant metasurfaces. *Science* **377**, 1215–1218 (2022).

42. H. Zhang, X. Sha, Q. Chen, J. Cheng, Z. Ji, Q. Song, S. Yu, S. Xiao, All-dielectric metasurface-enabled multiple vortex emissions. *Adv. Mater.* **34**, 2109255 (2022).

43. M. Kang, L. Mao, S. Zhang, M. Xiao, H. Xu, C. T. Chan, Merging bound states in the continuum by harnessing higher-order topological charges. *Light Sci. Appl.* **11**, 228 (2022).

44. M. Kang, S. Zhang, M. Xiao, H. Xu, Merging bound states in the continuum at off-high symmetry points. *Phys. Rev. Lett.* **126**, 117402 (2021).